

## Probing the antiferromagnetic structure of bilayer CrI<sub>3</sub> by second harmonic generation: A first-principles study

ZhenHua Li<sup>1</sup>, Zhi-Ming Yu<sup>2,3</sup>, JianHua Wei<sup>4,\*</sup> and Hong-Gang Luo<sup>1,†</sup>

<sup>1</sup>*School of Physical Science and Technology & Lanzhou Center for Theoretical Physics & Key Laboratory of Theoretical Physics of Gansu Province, Lanzhou University, Lanzhou 730000, China*

<sup>2</sup>*Centre for Quantum Physics, Key Laboratory of Advanced Optoelectronic Quantum Architecture and Measurement (MOE), School of Physics, Beijing Institute of Technology, Beijing 100081, China*

<sup>3</sup>*Beijing Key Lab of Nanophotonics & Ultrafine Optoelectronic Systems,*

*School of Physics, Beijing Institute of Technology, Beijing 100081, China*

<sup>4</sup>*Department of Physics, Renmin University of China, Beijing 100872, China*

 (Received 13 July 2022; revised 28 November 2022; accepted 29 November 2022; published 13 December 2022)

Two-dimensional antiferromagnetic materials with robust second harmonic generation (SHG) have been attracting significant research interest. In recent experiments, enhanced SHG from layered antiferromagnet (AFM) bilayer chromium trioxide (CrI<sub>3</sub>) with *A*-type antiferromagnetic order has been observed. However, bilayer CrI<sub>3</sub> with *A*-type, *C*-type, and *G*-type antiferromagnetic order may simultaneously occur in experimental synthesis, as the total free-energy difference between the three AFMs is small. Here, based on symmetry analysis and first-principles calculations, we study the three kinds of bilayer AFMs with and without the spin-orbit coupling (SOC) effect. We find that for all three types, the *i*-type SHG response vanishes due to the centrosymmetric lattice structure. However, significant *c*-type SHG response can arise in *A*-type and *C*-type AFMs but still vanishes for *G*-type AFM. Under normal incidence, both *A*-type and *C*-type AFMs exhibit three independent nonvanishing SHG components. Remarkably, the nonvanishing SHG components of *A*-type and *C*-type AFMs are mutually exclusive, namely, the SHG components that are finite for *A*-type vanish for *C*-type and vice versa. In particular, the SHG of both *A*-type and *C*-type AFMs is sensitive to the SOC effect and it becomes enhanced when the SOC effect is fully considered. Hence, the SHG response would be an efficient method for probing bilayer CrI<sub>3</sub> with different antiferromagnetic orders.

DOI: [10.1103/PhysRevB.106.235410](https://doi.org/10.1103/PhysRevB.106.235410)

### I. INTRODUCTION

Two-dimensional (2D) materials have attracted a lot of interest in current studies, as they exhibit many intriguing features compared to 3D bulk materials [1–8]. A unique feature of 2D materials is that a monolayer material can be vertically stacked to produce bilayer and few-layer material, and the physical properties of the system vary with the stacking way and the number of stacked layers. A trend in recent research is to push the study of 2D materials to magnetic systems, e.g., introducing magnetic ordering into 2D materials. Because the magnetic ordering breaks time-reversal symmetry ( $\mathcal{T}$ ), time-noninvariant quantities naturally arise, such as the anomalous Hall effect, sizable magnetic anisotropy [9], layer-dependent magnetic ordering states [10], and the Kosterlitz-Thouless phase transition [11]. Magnetic 2D materials open up a new platform for theoretical investigation and for realizing new functionalities.

Since the discovery of 2D CrI<sub>3</sub> [5] and Cr<sub>2</sub>Ge<sub>2</sub>Te<sub>6</sub> [6], which are the first two 2D intrinsic magnetic materials, many 2D magnetic materials have been predicted, and some of them

have been confirmed experimentally. Interestingly, it has been found that the ferromagnetism of 2D CrI<sub>3</sub> is layer-dependent. Specifically, monolayer CrI<sub>3</sub> is a ferromagnetic (FM) material with a Curie temperature of 45 K and out-of-plane spin orientation [5], while bilayer CrI<sub>3</sub> exhibits *A*-type antiferromagnetic (AFM) ordering in its ground state [8,12]. However, bilayer CrI<sub>3</sub> with two other magnetic configurations, namely *C*-type and *G*-type antiferromagnetic order, may also occur in experiments, as the total free-energy difference between the three types of the bilayer AFMs is small [13,14]. Therefore, it is crucial to find an efficient method to distinguish these AFM states.

Due to the ultralow thickness, the signal of traditional characterization methods is very weak in 2D materials. On the other hand, the thin films generally have high optical transparency, and the optical measurements become prevalent. For example, x-ray magnetic circular/linear dichroism (XMCD/XMLD) [15] and SHG play an increasingly important role in characterizing 2D magnetic materials. XMCD/XLCD is generally used to characterize the electronic magnetic structure in bulk materials, film materials, and heterostructures through the absorption difference of two-type polarized light under a magnetic field [16]. It is element-specific and surface/interface-sensitive. In contrast to XMCD/XLCD, SHG is crystalline-symmetry-sensitive

\*wjh@ruc.edu.cn

†luohg@lzu.edu.cn

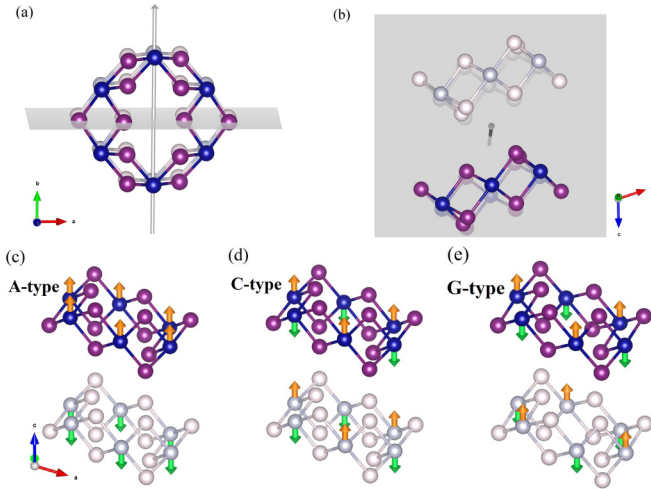


FIG. 1. The upper two figures [(a) the view along the  $c$ -axis and (b) the view along the  $y$ -axis] show the symmetry operators of monoclinic bilayer chromium tri-iodide. The axis is the twofold rotation operator  $C_{2y}$ , and the panel is the mirror plane operator  $M_y$ , which is normal to  $C_{2y}$ . The lower three figures show the three antiferromagnetic structures: (c)  $A$ -type, (d)  $C$ -type, and (e)  $G$ -type, respectively. For all the figures, a small rotation is applied to make all the atoms visible, and the same special hexagonal-like unit is used to plainly show the symmetry and the magnetic structures. The structures are produced by using VESTA [33].

[17], as well as surface/interface-sensitive [18]. Thus, SHG is powerful in determining symmetry-related physical phenomena in bulk, layered materials [4,19–24] and heterostructure materials [25,26]. Moreover, the SHG components that vanish in bulk materials can appear in corresponding layered materials [27], as the layered materials may have lower symmetry [23] compared with the bulk. For example, it was shown in a recent experiment [4] that while bulk  $\text{CrI}_3$  does not have a finite SHG effect due to the presence of  $\mathcal{P}$  symmetry, bilayer  $\text{CrI}_3$  with  $A$ -type antiferromagnetism exhibits enhanced nonreciprocal (time-noninvariant) SHG. Therefore, SHG promises to play an important role in exploring symmetry in ultrathin layered materials. Previous experimental work reveals that SHG can well discriminate between antiferromagnetic ordering and paramagnetic or ferromagnetic ordering [4]. Based on first-principles calculations, theoretical work shows that the different SHG responses can reflect different atomic and magnetic symmetries between different stack orderings for both bilayer and trilayer  $\text{CrI}_3$ , and between antiferromagnetic and ferromagnetic ordering for trilayer  $\text{CrI}_3$  [20].

Motivated by this recent progress, in this work, based on symmetry analysis and first-principles calculations, we systematically study the SHG of three kinds of bilayer van der Waals magnet  $\text{CrI}_3$  [28] with  $A$ -type,  $C$ -type, and  $G$ -type AFM order (see Fig. 1). We show that the three types exhibit completely different SHG responses. For all three types, the  $i$ -type SHG response vanishes due to the centrosymmetric lattice structure. However, for  $A$ -type and  $C$ -type AFM, the spatial inversion symmetry ( $\mathcal{P}$ ) is broken by the magnetic configurations, while  $G$ -type AFM remains  $\mathcal{P}$ -symmetric. As a result,  $c$ -type SHG response will arise in  $A$ -type and  $C$ -type AFM but still vanishes for  $G$ -type AFM. We analyze the vanishing-

nonvanishing components of the SHG susceptibility tensors for  $A$ -type and  $C$ -type AFM, and we find that both types exhibit three independent nonvanishing SHG components for normal incidence. Interestingly, the three independent nonvanishing SHG components for  $A$ -type and  $C$ -type AFM are mutually exclusive, e.g., the SHG component that is finite for  $A$ -type must vanish for  $C$ -type and vice versa. For  $A$ -type antiferromagnetic structure, our results produce the same symmetry property of the SHG as the recent experimental results [4], where  $\chi_{xxx}^{(2)}$ ,  $\chi_{yyy}^{(2)}$ ,  $\chi_{yxy}^{(2)} = \chi_{yyx}^{(2)}$  are the nonvanishing components when the light propagation is along the  $z$  axis. However, the order of magnitude in our calculations is larger than the experimental results.

We calculate the SHG of all three types of bilayer  $\text{CrI}_3$  with and without the SOC effect. We find that when the SOC effect is fully considered, the SHG for both  $A$ -type and  $C$ -type AFMs would be significantly enhanced, and it is about  $10^4$  times larger than that without the SOC effect. However, the conclusion of vanishing-nonvanishing SHG components and the mutual exclusion of SHG for  $A$ -type and  $C$ -type AFM still hold, as guaranteed by the symmetries of systems. The robust response and the sensitive dependence of symmetry make SHG an efficient method for identifying the magnetic configuration of bilayer  $\text{CrI}_3$  and other layered AFM materials. Hence, our work provides a useful guide to explore magnetic structures of 2D materials by using SHG.

## II. COMPUTATION METHOD

We employ the Vienna Ab initio Simulation Package (VASP) [29,30] to perform first-principle calculations within the Perdew-Burke-Ernzerhof (PBE) [31] parametrization of the projector-augmented-wave (PAW) [32] pseudopotential for the exchange-correlation functional based on the generalized-gradient approximation (GGA). To account for the correlation effects for Cr- $3d$  orbitals, the Hubbard  $U$  correction, 3 eV, is adopted and the magnetization  $\sim 3.2\mu_B$  is finally obtained for all three AFMs.

The cutoff energy is set as 300 eV. The energy convergence criterion is set to be  $10^{-6}$  eV. For the calculation of the  $\text{CrI}_3$  bilayer with all three AFM orders, a  $9 \times 9 \times 1$   $\Gamma$ -centered  $k$ -point mesh is used and a vacuum layer with a thickness of 22 Å is taken to avoid interaction between the two surfaces of one slab. The atom positions of the bilayer structure for the three AFM orders are fully relaxed until all the forces acting on the atoms are smaller than 0.03 eV/Å. For the different AFM orders, they have the same structure, including the atom positions and the interlayer distances. The SHG response coefficients are calculated using our code [34,35] with the electron structure information and the derivatives of the wave functions obtained from the output of VASP.

## III. CRYSTAL STRUCTURE AND MAGNETIC ORDERING

The bulk  $\text{CrI}_3$  exhibits two different crystalline structures, belonging to trigonal  $R\bar{3}$  (no. 148) and monoclinic  $C2/m$  (no. 12) space groups, respectively [36]. Therefore, the bilayer normal to the [001] direction has two stacking orders. However, they are connected by an in-panel shift [12]. Although

TABLE I. The total energy differences per chemical unit (three iodine atoms and one chromium atom) for three AFM structures in CrI<sub>3</sub> bilayer as shown in Figs. 1(c), 1(d), and 1(e). The energy of A-type AFM is used as the reference energy.

	$\Delta E_{C\text{-type}}$ (meV)	$\Delta E_{G\text{-type}}$ (meV)
PBE	25.60	25.62
PBE+SOC	27.52	27.56

$R\bar{3}$  can also be used to demonstrate our idea, here we chose the monoclinic  $C2/m$  stack order because there already exists an available experimental result from which the vanishing-nonvanishing SHG components can be found for A-type AFM [4]. As shown in Fig. 1, there can exist three types of AFM structures, i.e., A-type with interlayer AFM order, C-type with intralayer AFM order, and G-type with both interlayer and intralayer AFM order simultaneously. As listed in Table I, the total energies of the C-type AFM and G-type AFM are

approximately  $\sim 25$  meV per chemical unit higher than A-type AFM, and it can be seen that the difference between them is small. Thus, in material growth, the three types of bilayer CrI<sub>3</sub> may appear simultaneously [37].

The crystalline structure of bilayer CrI<sub>3</sub> belongs to point group  $2/m$  ( $C_{2h}$ ), which contains four symmetry operators, i.e., an identity operator, a twofold rotation operator  $C_{2y}$ , a spatial inversion operator  $\mathcal{P}$ , and a mirror plane  $M_y$  normal to the  $y$  direction, as shown in Figs. 1(a) and 1(b). By introducing magnetism, it is the magnetic point group instead of the point group that accounts for the symmetry analysis of bilayer CrI<sub>3</sub>.

(i) For A-type, the magnetic structure breaks  $\mathcal{P}$  and  $M_y$  but respects  $C_{2y}$ , as well as the product of  $\mathcal{P}$  ( $M_y$ ) and time-reversal symmetry  $\mathcal{T}$ , e.g.,  $\mathcal{PT}$  ( $M_y\mathcal{T}$ ). Hence, the bilayer CrI<sub>3</sub> with A-type AFM belongs to magnetic point group  $2/m'$ .

(ii) For C-type, the magnetic structure breaks  $\mathcal{P}$  and  $C_{2y}$  but respects  $M_y$ ,  $\mathcal{PT}$ , and  $C_{2y}\mathcal{T}$ . Hence, the bilayer CrI<sub>3</sub> with C-type AFM belongs to magnetic point group  $2'/m$ .

(iii) For G-type, the magnetic structure keeps all the symmetry operators  $\mathcal{P}$ ,  $M_y$ , and  $C_{2y}$ . Hence, the bilayer CrI<sub>3</sub> with

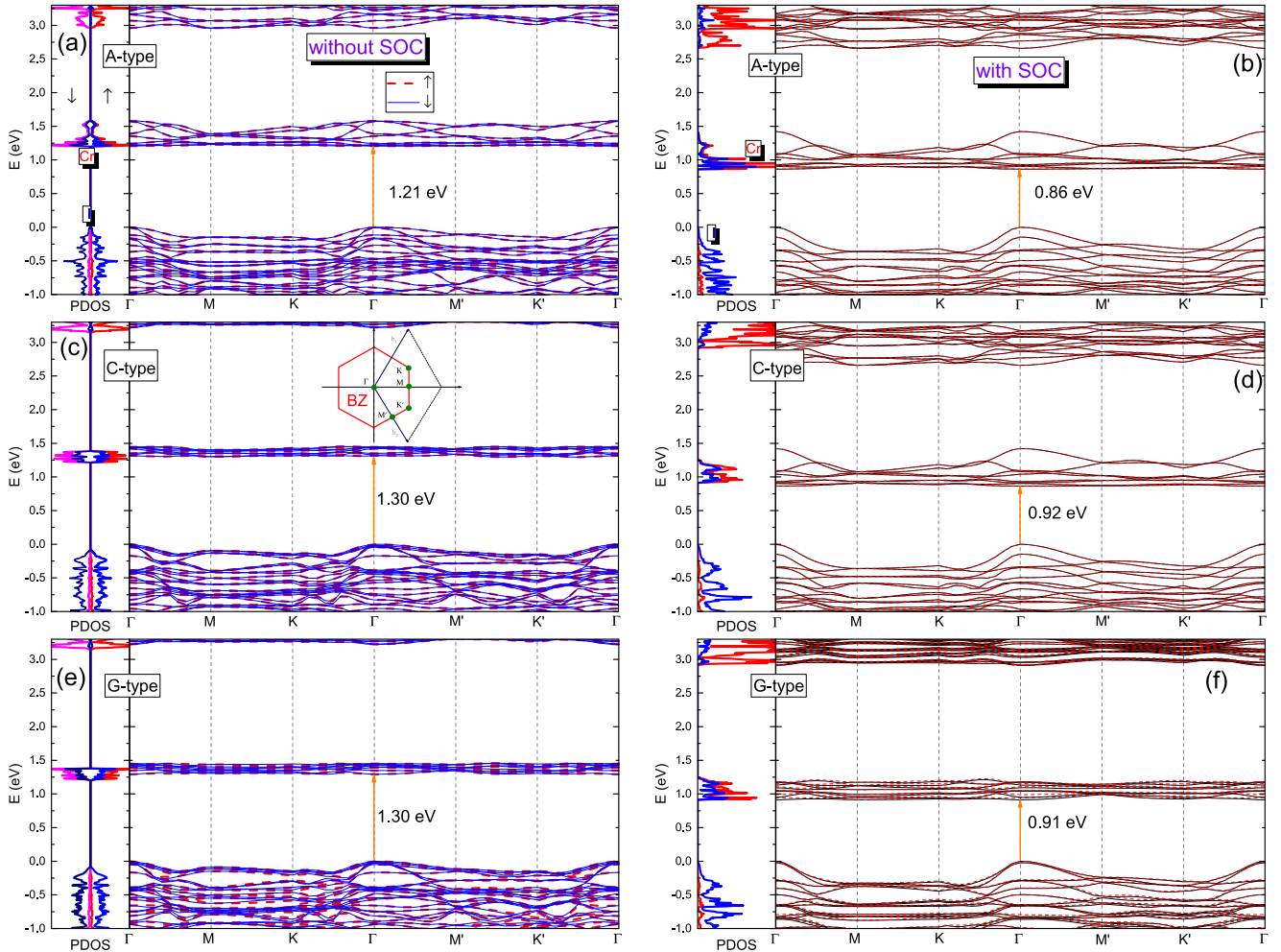


FIG. 2. Band structures of bilayer CrI<sub>3</sub> with three types of AFM order, associated with the projected density of states. Parts (a), (c), and (e) show the results without the SOC effect, and (b), (d), and (f) present the results with the SOC effect. For all three of the magnetic structures, the valence bands mainly come from the  $p$  orbital of I, while the conduction band comes from the  $d$  orbital of Cr. The band gaps are almost the same, either for cases without SOC or those with SOC. The BZ and the high-symmetry points of bilayer CrI<sub>3</sub> are indicated in the inset of Fig. 2(c).

G-type AFM belongs to the magnetic point group  $2/m$ . In particular, the  $\mathcal{P}$  makes all the SHG components vanish.

As explicitly shown in the following, due to the difference in symmetry, the three kinds of bilayer  $\text{CrI}_3$  would exhibit completely different SHG responses.

#### IV. ELECTRONIC BAND STRUCTURE

We first study the electronic band structures of the three kinds of AFM bilayer  $\text{CrI}_3$ . The calculated band structures without and with SOC are plotted in Fig. 2. The Brillouin zone (BZ) of bilayer  $\text{CrI}_3$  and the high symmetric points are indicated in the inset of Fig. 2(c). Notice that the high-symmetry points  $K'$  and  $M'$  are not equivalent to  $K$  and  $M$ , due to the absence of  $C_{3z}$  rotation symmetry for the bilayer  $\text{CrI}_3$  studied here. This can also be found by examining the band structure (see Fig. 2).

One finds that the three AFM materials are insulators with a slight difference in the band gaps, which are 1.21, 1.30, and 1.30 eV when SOC is neglected and decrease to 0.86, 0.96, and 0.91 eV by including the SOC effect for A-, C-, and G-type, respectively. These results are consistent with the previous calculations [12]. Moreover, from the projected density of states (PDOS), we find that for all three bilayer  $\text{CrI}_3$ , the valence states are mostly contributed by the  $p$  orbital of I atoms, while the conduction states are mainly from the  $d$  orbital of Cr atoms. The similarity of the electronic band structures will lead to similar electronic, magnetic, and transport properties for the three AFMs. Hence, it is difficult to distinguish them by many measurements that are not sensitive to magnetic symmetry.

#### V. FIRST-ORDER SUSCEPTIBILITY

We calculate the first-order susceptibilities for different antiferromagnetic structures in bilayer chromium tri-iodide with and without SOC. The first-order susceptibility is an intuitive insight to understand the optical properties including the SHG [38]. The empirical Miller's rule gives the relationship [39,40] of the SHG in terms of the first-order susceptibilities as

$$\chi_{abc}^{(2)}(2\omega) = \alpha \chi_{aa}^{(1)}(2\omega) \chi_{bb}^{(1)}(\omega) \chi_{cc}^{(1)}(\omega), \quad (1)$$

where  $\alpha$  is a constant, and  $a, b, c$  are Cartesian indices. This expression is valid in most materials.

The results can be found in Figs. 3(a) and 3(b). When the SOC is excluded, the bilayer chromium tri-iodide exhibits a uniaxial crystal where the in-panel optical property is isotropic,  $\chi_{xx}^{(1)}(\omega) = \chi_{yy}^{(1)}(\omega)$ . The C-type AFM bilayer and G-type AFM one almost have the same first-order susceptibility, while the A-type AFM structure has a slight difference; see Fig. 3(a). When the SOC is included, the in-panel isotropy is broken down, while the similarity between C-type AFM and G-type AFM still nearly holds, but the magnitude is enlarged by four orders for both magnetic structures, as shown in Fig. 3(b). For the A-type AFM structure, the  $\chi_{xx}^{(1)}(\omega)$  and  $\chi_{yy}^{(1)}(\omega)$  are also enlarged by almost six and seven orders, respectively. Although the sharply increased magnitude of the first-order susceptibilities is questionable (see the last part for further discussion), it is somewhat indicative that some of the SHG components have very large intensity according to

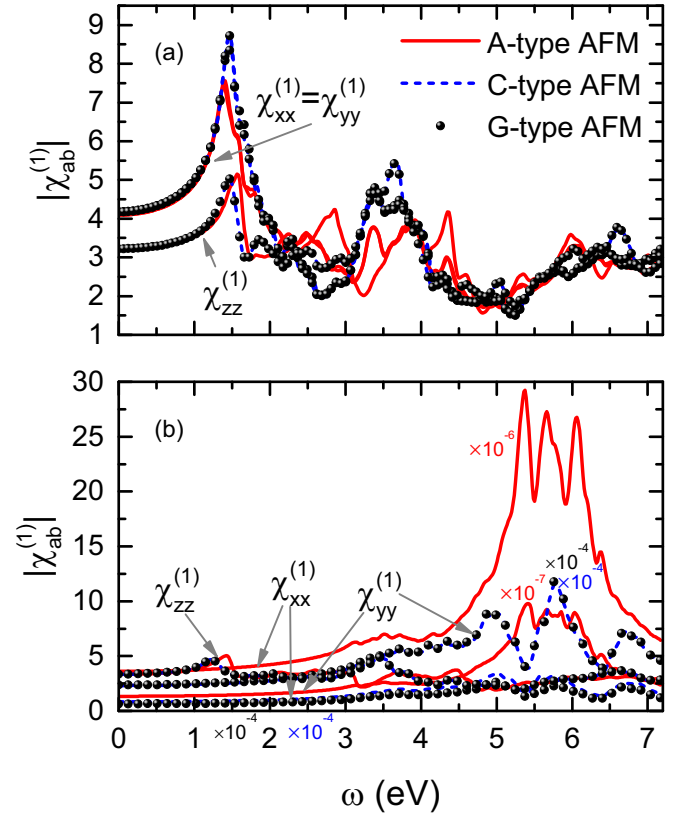


FIG. 3. The first-order susceptibilities without (a) and with (b) SOC for different AFM structures in bilayer chromium tri-iodide. For the case with SOC, in (b), each of the magnitudes of  $\chi_{xx}^{(1)}(\omega)$  and  $\chi_{yy}^{(1)}(\omega)$  for all three types of AFM is scaled by a factor alongside the curve with the same color. SOC breaks down the in-panel isotropy and sharply enhances the magnitudes of  $\chi_{xx}^{(1)}(\omega)$  and  $\chi_{yy}^{(1)}(\omega)$  for all three AFMs.

Miller's rule when SOC is included. However, in contrast to the other components, the  $\chi_{zz}^{(1)}(\omega)$  for three AFMs has little change. The differences in magnitude are hard to detect in experiments. Therefore, the first-order susceptibility is not a practicable quantity to distinguish the different magnetic structures.

#### VI. SHG RESPONSES

Since the SHG is sensitive to the symmetry, it is widely used to characterize symmetries of crystallographic structure [17,41]. When traveling through a medium, the electromagnetic waves can induce many multipole moments, such as electric polarization and magnetization, which in turn compose the source term of the output waves. Generally, the electric-dipole (ED), which is in proportion to electric polarization, is the leading contribution to the source. Hence, the SHG is fundamentally generated by the polarization of the electrons, which is constrained by the symmetry of both the crystallographic structure and the magnetic structure of crystals.

The photoinduced nonlinear polarization  $\mathbf{P}(2\omega)$  is expressed as

$$P_a(2\omega) = \epsilon_0 \chi_{abc}^{(2)} E_b(\omega) E_c(\omega), \quad (2)$$

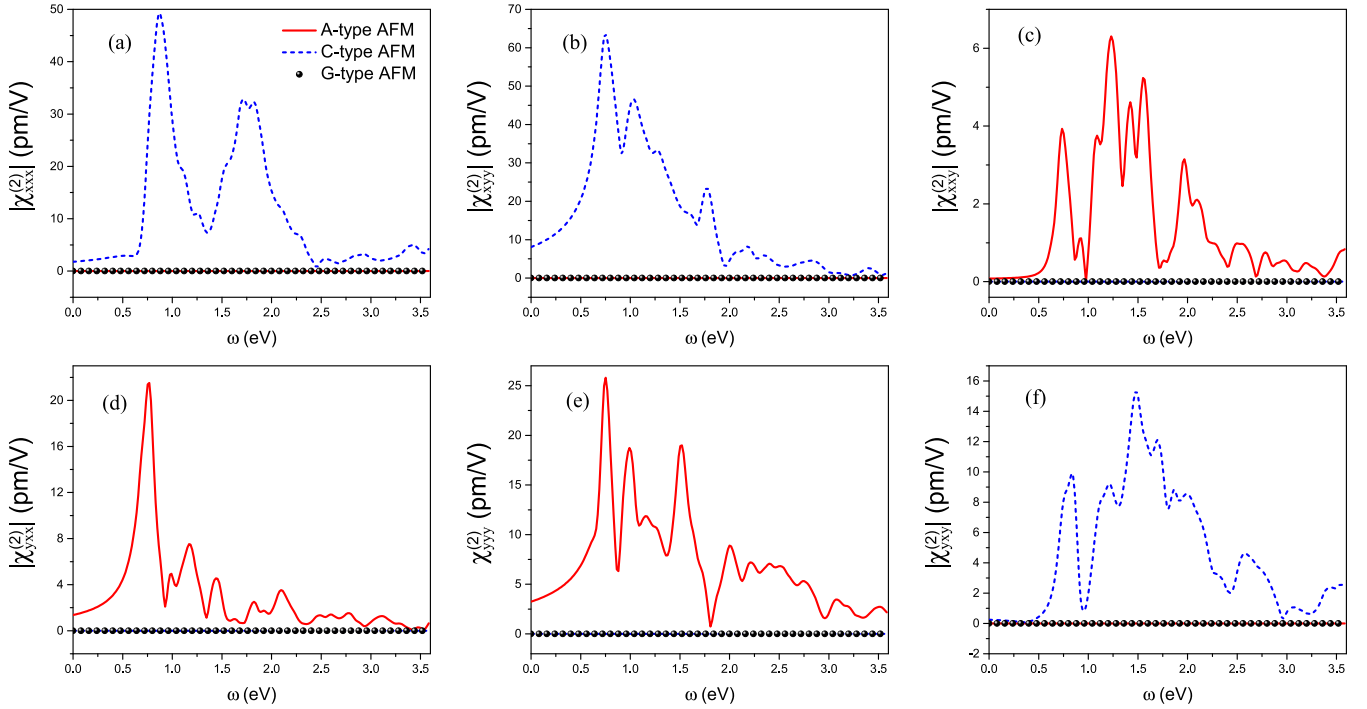


FIG. 4. The SHG components of in-panel polarization without SOC for different antiferromagnetic structures in bilayer chromium triiodide with a  $2/m$  crystallographic point group and different magnetic point groups. These shown components are mutually exclusive for A-type AFM and C-type AFM, while all the components of G-type AFM are zero.

with  $\epsilon_0$  the vacuum permittivity,  $\chi_{abc}^{(2)}$  the SHG tensor,  $\mathbf{E}$  the electric field of the light,  $\omega$  the light frequency, and  $a, b, c$  are Cartesian indices. The SHG tensor under ED approximation can be divided into two parts,

$$\chi_{abc}^{(2)} = \chi_{abc}^i + \chi_{abc}^c, \quad (3)$$

where  $\chi_{abc}^i$  is invariant under  $\mathcal{T}$  symmetry while  $\chi_{abc}^c$  is not invariant under  $\mathcal{T}$  symmetry.  $\chi_{abc}^i$  and  $\chi_{abc}^c$  are termed as  $i$ -type and  $c$ -type SHG tensors, respectively. It can be easily found that when the system has  $\mathcal{P}$  symmetry, both  $\chi_{abc}^i$  and  $\chi_{abc}^c$  vanish. Moreover,  $\chi_{abc}^i$  and  $\chi_{abc}^c$  are, respectively, determined by the crystallographic and magnetic structure of the crystal [41]. Hence,  $\chi_{abc}^i$  would vanish when the crystallographic structure of the system is centrosymmetric. In contrast,  $\chi_{abc}^c$  vanishes when the crystal is paramagnetic, which also indicates  $\chi_{abc}^c$  generally is proportional to the magnetic order parameter [42]. As discussed above, the magnetization of Cr atoms for the three AFMs is  $3.2\mu_B$ , which is quite large. Hence, one can expect that significant SHG may be observed in bilayer AFM  $\text{CrI}_3$ .

We note that for three AFMs, the crystallographic structure is centrosymmetric, indicating that  $\chi_{abc}^i$  must vanish. However, the magnetic ordering can break  $\mathcal{P}$  symmetry, allowing the appearance of  $\chi_{abc}^c$ . For simplification, we consider normal incidence, i.e., the propagation direction of the incident light is normal to the sample, which is favorable for experimental detection. Then, by symmetry analysis, we find that both A-type and C-type only have three nonvanishing independent SHG components. Explicitly, the three SHG components for A-type are  $\chi_{yxx}^{(2)}$ ,  $\chi_{yyy}^{(2)}$ , and  $\chi_{xxy}^{(2)} = \chi_{yyx}^{(2)}$ , and for C-type they are  $\chi_{xxx}^{(2)}$ ,  $\chi_{xyy}^{(2)}$ , and  $\chi_{xyx}^{(2)} = \chi_{yyx}^{(2)}$ . Interestingly, one finds that the

SHG component here that is finite for A-type must vanish for C-type, and vice versa. For G-type, all the SHG components must be zero, as it remains  $\mathcal{P}$ -symmetric.

Generally, the SHG tensor  $\chi_{abc}^{(2)}$  can be divided into three parts [43,44]:

$$\chi_{abc}^{(2)} = \zeta_{abc}^{(2)} + \eta_{abc}^{(2)} + \sigma_{abc}^{(2)}, \quad (4)$$

where  $\zeta_{abc}^{(2)}$  and  $\eta_{abc}^{(2)}$  denote the interband transitions and the intraband transitions, respectively, and  $\sigma_{abc}^{(2)}$  describes the modulation of the interband terms by the intraband terms  $\sigma_{abc}^{(2)}$  [43,44]. Here, due to the centrosymmetry crystallographic structure, we have  $\chi_{abc}^i = 0$  and  $\chi_{abc}^{(2)} = \chi_{abc}^c$  for all three AFMs. In the calculations, the SHG components are calculated from the symmetrized position matrix [44], e.g., the constraints from symmetry operators have been imposed on the position matrices. Moreover, we have used the perturbation expansion after discretization (PEAD) [45] to obtain precise position matrices. The calculated results of SHG components associated with the in-plane polarized harmonic light are shown in Fig. 4 (without SOC) and Fig. 5 (with SOC). The obtained nonvanishing SHG components are consistent with the above symmetry analysis.

For A-type and C-type AFM, the breaking of centrosymmetry allows the nonvanishing SHG to appear. One should be careful in the VASP implementation of calculating the momentum matrix. If the derivatives of the orbitals are obtained by solving the linear Sternheimer equation suggested as the density functional perturbation theory [46], the components that must be vanished will not be exactly zero. This problem can be resolved by the PEAD method [45], which is validated by the fact that the components that should be zero became

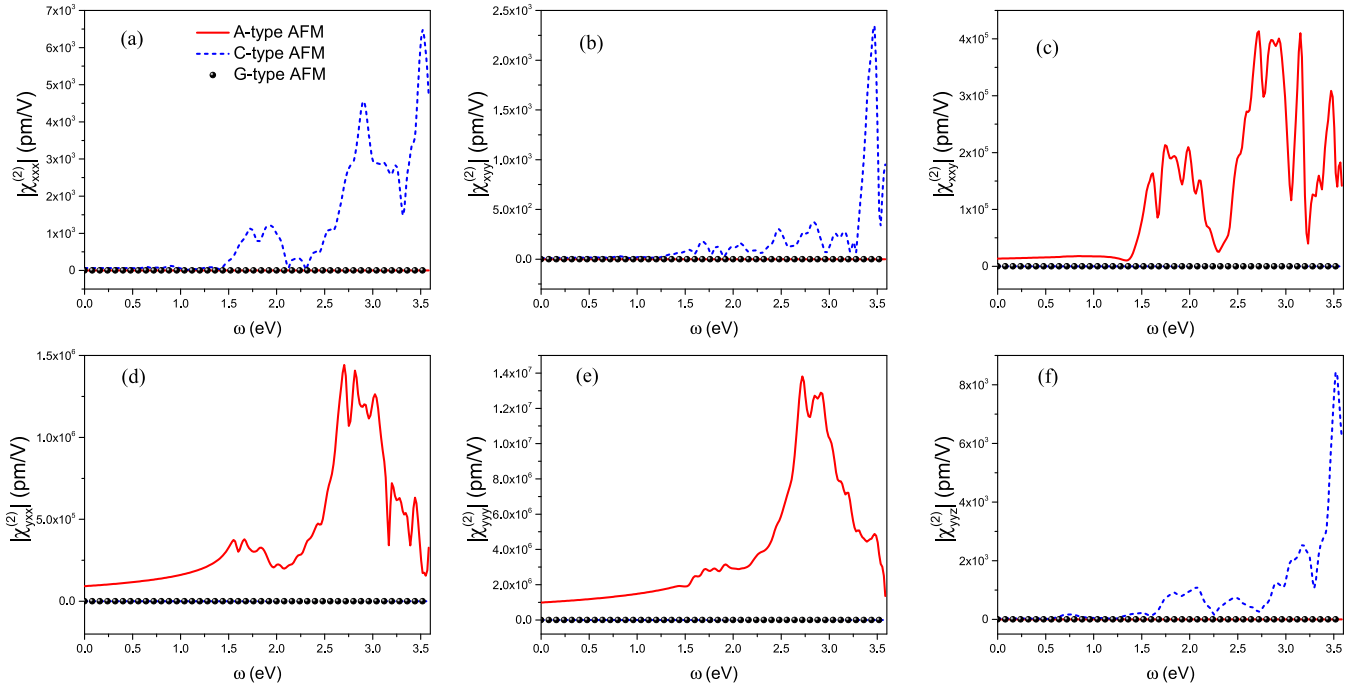


FIG. 5. The same SHG components as that in Fig. 4 but with SOC. The magnitudes are dramatically enhanced compared to the case without SOC. However, the mutual exclusion for A-type AFM and C-type AFM, and the vanishing-nonvanishing components, still hold on.

exactly zero even in spin-polarized calculation when SOC is absent. Furthermore, the symmetrized position matrix by the operators of the corresponding magnetic point group can give more accurate results.

From the calculated SHG without SOC (see Fig. 4), one finds that all the SHG components are consistent with the symmetries of the magnetic point group, and the nonvanishing components are almost in the same order of magnitude as that of the SHG in bulk materials. In contrast, when the SOC effect is included, the magnitudes of the nonvanishing SHG are significantly enhanced, as shown in Fig. 5. Although the magnitudes have changed dramatically, the vanishing-nonvanishing components still remain for the three types of AFM. The mutual exclusion for A-type AFM and C-type AFM is also the same as the case without SOC. Although the G-type AFM has all vanishing SHG components, which is similar to that of ferromagnetic and nonmagnetic bilayer  $\text{CrI}_3$ , it can be easily distinguished by the macroscopic magnetic susceptibilities. Thus the vanishing-nonvanishing components provide a robust tool to distinguish the magnetic structures of bilayer  $\text{CrI}_3$ . However, the mechanism of enhanced SHG intensity has not been reported so far. It may be related to the breakdown of the spin-conserved optical selection rule by the SOC, and more excitations with a combination of momentum and spin indices are allowed [47].

In experiments, the polarization-resolved SHG is a popular characterization technique for probing the symmetries [17]. Different symmetries of the materials exhibit different petal-like SHG patterns. Therefore, we produce the polarization-resolved SHG of bilayer  $\text{CrI}_3$  without and with SOC in Figs. 6 and 7 for A-type and C-type AFM at two typical light frequencies: 900 nm (1.376 eV) and 1064 nm (1.168 eV), where the latter is easily accessible for a commercial Nd:YAG laser.

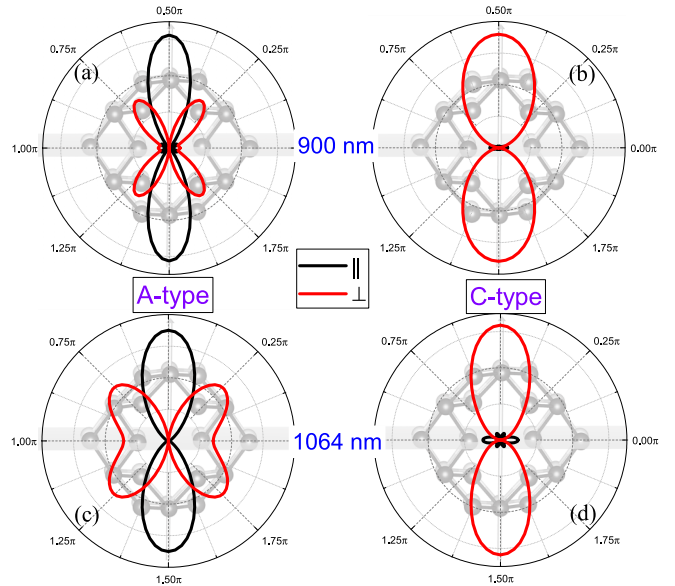


FIG. 6. The calculated polarization-resolved SHG patterns  $|E_{||}|^2$  and  $|E_{\perp}|^2$  as a function of azimuthal polarization at both 900 nm (1.376 eV, top row) and 1064 nm (1.168 eV, bottom row) for A-type AFM in (a) and (c), and for C-type AFM in (b) and (d). The different colors represent the polarization directions of harmonic light, which are parallel (black) and perpendicular (red) to the polarization direction of incident light, respectively. The zero nodal point of  $|E_{||}|^2$  shows up at  $\varphi = 0$  for A-type, and  $\varphi = \pm\pi/2$  for C-type, while the zero nodal point of  $|E_{\perp}|^2$  shows up at  $\varphi = \pm\pi/2$  for A-type and  $\varphi = 0$  for C-type.

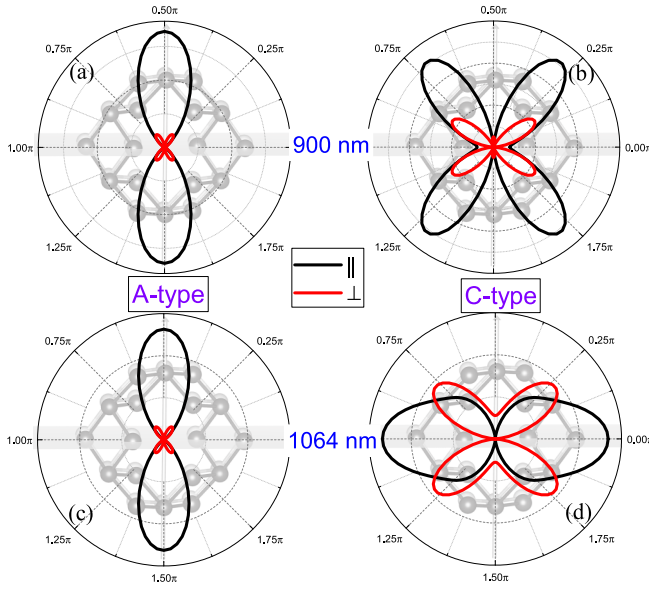


FIG. 7. The calculated polarization-resolved SHG patterns  $|E_{\parallel}|^2$  and  $|E_{\perp}|^2$  as the same as Fig. 6 but including the SOC effect. The zero nodal point of  $|E_{\parallel}|^2$  is still located at  $\varphi = 0$  for A-type and  $\varphi = \pm\pi/2$  for C-type, while  $|E_{\perp}|^2$  at  $\varphi = \pm\pi/2$  for A-type, and at  $\varphi = 0$  for C-type.

With normal incidence, the polarization of the light is in-plane, i.e., the  $x$ - $y$  plane, and the polarization direction can be described by an azimuthal angle  $\varphi$  with respect to a reference direction, which here is the  $x$  direction, as shown in Fig. 1 or in the polarization-resolved SHG patterns in Figs. 6 and 7. The polarization direction of the generated second harmonic light can be perpendicular or parallel to the polarization direction of the incident light. Then the relation between the input and output electric fields can be rewritten as

$$E_{\parallel}(2\omega) \propto P_x(2\omega) \cos \varphi + P_y(2\omega) \sin \varphi, \quad (5)$$

$$E_{\perp}(2\omega) \propto -P_x(2\omega) \sin \varphi + P_y(2\omega) \cos \varphi. \quad (6)$$

For A-type AFM,

$$E_{\parallel} \propto (\chi_{yxx}^{(2)} + 2\chi_{xxy}^{(2)}) \cos^2 \varphi \sin \varphi + \chi_{yyy}^{(2)} \sin^3 \varphi, \quad (7)$$

$$E_{\perp} \propto \chi_{yxx}^{(2)} \cos^3 \varphi + (\chi_{yyy}^{(2)} - 2\chi_{xxy}^{(2)}) \cos \varphi \sin^2 \varphi \quad (8)$$

and for C-type AFM,

$$E_{\parallel} \propto \chi_{xxx}^{(2)} \cos^3 \varphi + (\chi_{xyy}^{(2)} + 2\chi_{xyx}^{(2)}) \cos \varphi \sin^2 \varphi, \quad (9)$$

$$E_{\perp} \propto (2\chi_{xyx}^{(2)} - \chi_{xxx}^{(2)}) \cos^2 \varphi \sin \varphi - \chi_{xyy}^{(2)} \sin^3 \varphi. \quad (10)$$

Here,  $E_{\parallel}(2\omega)$  and  $E_{\perp}(2\omega)$  denote the parallel and perpendicular polarization of the second harmonic output field regarding that of the input light, respectively.

From the calculated  $|E_{\parallel}|^2$  and  $|E_{\perp}|^2$  of the two AFM types in Fig. 6 for the case without SOC and Fig. 7 for the case with SOC, we find the polarization-resolved SHG patterns are very similar, which have two-lobed or four-lobed features because of the twofold symmetry for  $C_{2y}$  of A-type AFM and  $M_y$  of C-type AFM. However, the polarization-resolved SHG patterns of A-type and C-type also have some differences due

to the different magnetic structures. For A-type AFM, under symmetry  $C_{2y}$ ,  $P_x \rightarrow -P_x$  and  $P_y \rightarrow P_y$ . Therefore, when  $E_{\parallel} \parallel P_x$  or  $E_{\perp} \parallel P_x$ ,  $C_{2y}$  symmetry requires the corresponding zero nodal point  $|E_{\parallel}|^2 = 0$  or  $|E_{\perp}|^2 = 0$  present at  $\varphi = 0$  or  $\varphi = \pm\pi/2$ , respectively. By contrast, for C-type AFM, under symmetry  $M_y$ ,  $P_x \rightarrow P_x$  and  $P_y \rightarrow -P_y$ . Therefore, when  $E_{\parallel} \parallel P_y$  or  $E_{\perp} \parallel P_y$ ,  $M_y$  symmetry requires the corresponding zero nodal point  $|E_{\parallel}|^2 = 0$  or  $|E_{\perp}|^2 = 0$  presenting at  $\varphi = \pm\pi/2$  or  $\varphi = 0$ , respectively. The zero nodal points can also be recognized from the trigonometric functions in Eqs. (7)–(10). The  $\varphi$  values of zero nodal points are guaranteed by the symmetry of the corresponding magnetic point groups, and they are irrelevant to whether SOC is included or not. Based on the knowledge of crystalline structure [48,49], the magnetic structures can also be easily recognized in experiments from the polarization-resolved SHG patterns.

## VII. DISCUSSIONS AND CONCLUSION

We want to point out that there exist several deficiencies in our calculations, which may affect the accuracy of amplitudes of the SHG responses. First, the GGA/LDA calculations usually underestimate the band gaps due to neglecting the many-body electron interaction. The accurate calculation needs to include many-body self-energy correction. The HSE hybrid functional or  $GW$  quasiparticle calculation is a useful method to consider the corrected band gap. In the  $GW$  calculation, it gives a self-energy correction 1.77 eV [50] and a direct quasiparticle gap of 2.59 eV [51] for ferromagnetic monolayer  $\text{CrI}_3$ . Therefore, the band gap of the AFM bilayer  $\text{CrI}_3$  should be larger than 2 eV. The change of the band gap will considerably change the SHG values and shape. However, it only significantly changes the SHG in the low-energy region, close to the band gap, while the SHG in the high-energy region has a minor change. Second, even with the correct band gap, the SHG will still deviate from the realistic values. The momentum matrix also needs to be calculated by taking into account the self-energy correction. However, it is extremely difficult for the HSE/ $GW$  method because the complex many-body wave functions are involved. Besides, in low dimensional materials, the strong excitonic effect is dominant in optical processes [51,52]. For current DFT calculations, it is almost impossible to obtain accurate SHG values by including all the effects. An alternative choice is to take the scissor shift to the lowest-energy exciton peak obtained from the Bethe-Salpeter equation. The scissor correction usually shifts the SHG curve and changes the magnitude while the profile is kept. As a result, this will largely change the SHG in the low-energy region but will produce the correct result at higher energies. Fortunately, the vanishing-nonvanishing components studied in this work are independent of these factors as no symmetry can be broken by the many-body interaction.

Besides, as for the magnitude of the SHG, there exists a problem that should be further investigated. In some first-principles calculations, including our present one, the magnitude of the SHG is usually much larger than the experimental result [20,53]. If the reduction of the band gap is considered due to the excitonic effect, the magnitude will further increase. In our calculation, the first-order susceptibilities are also incredibly large. We check these calculations,

and we find that it stems from simultaneously considering the SOC and the Berry-phase-based polarization to calculate the momentum matrix, which is obtained from the direct derivative with respect to the wave vector  $k$ . If the momentum matrices are obtained in an alternative way, such as solving the linear Sternheimer equation, the SOC indeed will change the first-order susceptibility and enhance the SHG, here less than 10 times the one without SOC for  $A$ -type AFM  $\text{CrI}_3$ , but not so large as several orders of magnitude. The answer to this problem is beyond our present scope and not essential for our current study.

To conclude, in this work we discuss the SHG in the centrosymmetric crystallographic structure with  $\text{CrI}_3$  bilayer, in which the  $i$ -type SHG is zero and  $c$ -type SHG appears due to the breaking of spatial inversion in  $A$ -type and  $C$ -type antiferromagnetic structures. We use both symmetry analysis and first-principles calculation to study the different SHG responses for different magnetic structures. We conclude that both the vanishing-nonvanishing SHG components and zero nodal points of polarization-resolved SHG patterns can be used to distinguish the different magnetic structures in centrosymmetric crystallographic layer structure.

For the noncentrosymmetric layer magnets, besides modulating the  $i$ -type SHG, which is contributed by the noncentrosymmetric crystallographic structure, the different antiferromagnetic structures, belonging to different magnetic point groups, will break different spatial-symmetry operators, thus some  $c$ -type SHG components can emerge, which vanish in the corresponding ferromagnetic ordering (e.g., under external magnetic field) or nonmagnetic ordering with the same crystallographic structure. This can also be used to identify the antiferromagnetic structures. Hence, due to the strong signal, SHG can provide a powerful and robust tool to probe the magnetic structures of layered dimensional materials that possess different magnetic point groups.

### ACKNOWLEDGMENTS

We acknowledge the financial support of NSFC (Grants No. 12004035, No. 11774418, No. 11834005, and No. 12047501). We also acknowledge the support of the Supercomputing Center of Lanzhou University.

- [1] A. H. Castro Neto, F. Guinea, N. M. R. Peres, K. S. Novoselov, and A. K. Geim, The electronic properties of graphene, *Rev. Mod. Phys.* **81**, 109 (2009).
- [2] Z.-M. Yu, S. Guan, X.-L. Sheng, W. Gao, and S. A. Yang, Valley-Layer Coupling: A New Design Principle for Valleytronics, *Phys. Rev. Lett.* **124**, 037701 (2020).
- [3] A. Bedoya-Pinto, J.-R. Ji, A. K. Pandeya, P. Gargiani, M. Valvidares, P. Sessi, J. M. Taylor, F. Radu, K. Chang, and S. S. P. Parkin, Intrinsic 2D-XY ferromagnetism in a van der Waals monolayer, *Science* **374**, 616 (2021).
- [4] Z. Y. Sun, Y. F. Yi, T. C. Song, G. Clark, B. Huang, Y. W. Shan, S. Wu, D. Huang, C. L. Gao, Z. H. Chen, M. McGuire, T. Cao, D. Xiao, W.-T. Liu, W. Yao, X. D. Xu, and S. W. Wu, Giant non-reciprocal second-harmonic generation from antiferromagnetic bilayer  $\text{CrI}_3$ , *Nature (London)* **572**, 497 (2019).
- [5] B. Huang, G. Clark, E. Navarro-Moratalla, D. R. Klein, R. Cheng, K. L. Seyler, D. Zhong, E. Schmidgall, M. A. McGuire, D. H. Cobden, W. Yao, D. Xiao, P. Jarillo-Herrero, and X. D. Xu, Layer-dependent ferromagnetism in a van der Waals crystal down to the monolayer limit, *Nature (London)* **546**, 270 (2017).
- [6] C. Gong, L. Li, Z. L. Li, H. W. Ji, A. Stern, Y. Xia, T. Cao, W. Bao, C. Z. Wang, Y. Wang, Z. Q. Qiu, R. J. Cava, S. G. Louie, J. Xia, and X. Zhang, Discovery of intrinsic ferromagnetism in two-dimensional van der Waals crystals, *Nature* **546**, 265 (2017).
- [7] Y. J. Deng, Y. J. Yu, Y. C. Song, J. Z. Zhang, N. Z. Wang, Z. Y. Sun, Y. F. Yi, Y. Z. Wu, S. W. Wu, J. Y. Zhu, J. Wang, X. H. Chen, and Y. B. Zhang, Gate-tunable room-temperature ferromagnetism in two-dimensional  $\text{Fe}_3\text{GeTe}_2$ , *Nature (London)* **563**, 94 (2018).
- [8] S. W. Jiang, J. Shan, and K. F. Mak, Electric-field switching of two-dimensional van der Waals magnets, *Nat. Mater.* **17**, 406 (2018).
- [9] N. D. Mermin and H. Wagner, Absence of Ferromagnetism or Antiferromagnetism in One- or Two-Dimensional Isotropic Heisenberg Models, *Phys. Rev. Lett.* **17**, 1133 (1966).
- [10] P. C. Hohenberg, Existence of Long-Range Order in One and Two Dimensions, *Phys. Rev.* **158**, 383 (1967).
- [11] J. M. Kosterlitz and D. J. Thouless, Ordering, metastability and phase transitions in two-dimensional systems, *J. Phys. C* **6**, 1181 (1973).
- [12] P. H. Jiang, C. Wang, D. C. Chen, Z. C. Zhong, Z. Yuan, Z.-Y. Lu, and W. Ji, Stacking tunable interlayer magnetism in bilayer  $\text{CrI}_3$ , *Phys. Rev. B* **99**, 144401 (2019).
- [13] A. Ray and T. Maitra, Nature of transport gap and magnetic order in zircon and scheelite type  $\text{DyCrO}_4$  from first principles, *J. Phys.: Condens. Matter* **27**, 105501 (2015).
- [14] C. He, Z. J. Ma, B.-Z. Sun, Q. Li, and K. C. Wu, Ab-initio study on the electronic, optical and ferroelectric properties of  $\text{LiOsO}_3$ , *Comput. Mater. Sci.* **105**, 11 (2015).
- [15] J. Stöhr, Exploring the microscopic origin of magnetic anisotropies with X-ray magnetic circular dichroism (XMCD) spectroscopy, *J. Magn. Magn. Mater.* **200**, 470 (1999).
- [16] P. Carra, B. T. Thole, M. Altarelli, and X. Wang, X-Ray Circular Dichroism and Local Magnetic Fields, *Phys. Rev. Lett.* **70**, 694 (1993).
- [17] H.-Y. Ye, Y.-Y. Tang, P.-F. Li, W.-Q. Liao, J. X. Gao, X. N. Hua, H. Cai, P.-P. Shi, Y.-M. You, and R.-G. Xiong, Metal-free three-dimensional perovskite ferroelectrics, *Science* **361**, 151 (2018).
- [18] R. P. Pan, H. D. Wei, and Y. R. Shen, Optical second-harmonic generation from magnetized surfaces, *Phys. Rev. B* **39**, 1229 (1989).
- [19] C. Wang, X. Liu, L. Kang, B.-L. Gu, Y. Xu, and W. Duan, First-principles calculation of nonlinear optical responses by Wannier interpolation, *Phys. Rev. B* **96**, 115147 (2017).
- [20] W. Song, R. Fei, L. Zhu, and L. Yang Nonreciprocal second-harmonic generation in few-layer chromium triiodide, *Phys. Rev. B* **102**, 045411 (2020).
- [21] Y. H. Shen, Y. G. Guo, and Q. Wang, Large out-of-plane second harmonic generation susceptibility in Penta- $\text{ZnS}_2$  sheet, *Adv. Theory Simul.* **3**, 2000027 (2020).

- [22] S. X. Wang, X. H. Cui, C. E. Jian, H. W. Cheng, M. M. Niu, J. Yu, J. X. Yan, and W. Huang, Stacking-engineered heterostructures in transition metal dichalcogenides, *Adv. Mater.* **33**, 2005735 (2021).
- [23] X. P. Fan, Y. Jiang, X. J. Zhuang, H. J. Liu, T. Xu, W. H. Zheng, P. Fan, H. L. Li, X. P. Wu, X. L. Zhu, Q. L. Zhang, H. Zhou, W. Hu, X. Wang, L. T. Sun, X. F. Duan, and A. L. Pan, Broken symmetry induced strong nonlinear optical effects in spiral WS<sub>2</sub> nanosheets, *ACS Nano* **11**, 4892 (2017).
- [24] J. Yu, X. F. Kuang, J. Z. Li, J. H. Zhong, C. Zeng, L. K. Cao, Z. W. Liu, Z. X. X. S. Zeng, Z. Y. Luo, T. C. He, A. L. Pan, and Y. P. Liu, Giant nonlinear optical activity in two-dimensional palladium diselenide, *Nat. Commun.* **12**, 1083 (2021).
- [25] Z. X. S. Zeng, X. X. Sun, D. L. Zhang, W. H. Zheng, X. P. Fan, M. He, T. Xu, L. T. Sun, X. Wang, and A. L. Pan, Controlled vapor growth and nonlinear optical applications of large-area 3R phase WS<sub>2</sub> and WSe<sub>2</sub> atomic layers, *Adv. Funct. Mater.* **29**, 1806874 (2019).
- [26] B. Jin, F. Liang, Z.-Y. Hu, P. Wei, K. L. Liu, X. Z. Hu, G. V. Tendeloo, Z. S. Lin, H. Q. Li, X. Zhou, Q. H. Xiong, and T. Y. Zhai, Nonlayered CdSe flakes homojunctions, *Adv. Funct. Mater.* **30**, 1908902 (2020).
- [27] A. Kirilyuk and T. Rasing, Magnetization-induced-second-harmonic generation from surfaces and interfaces, *J. Opt. Soc. Am. B* **22**, 148 (2005).
- [28] N. Samarth, Magnetism in flatland, *Nature (London)* **546**, 216 (2017).
- [29] G. Kresse and J. Furthmüller, Efficient iterative schemes for ab initio total-energy calculations using a plane-wave basis set, *Phys. Rev. B* **54**, 11169 (1996).
- [30] G. Kresse and D. Joubert, From ultrasoft pseudopotentials to the projector augmented-wave method, *Phys. Rev. B* **59**, 1758 (1999).
- [31] J. P. Perdew, K. Burke, and M. Ernzerho, Generalized Gradient Approximation Made Simple, *Phys. Rev. Lett.* **77**, 3865 (1996).
- [32] P. E. Blöchl, Projector augmented-wave method, *Phys. Rev. B* **50**, 17953 (1994).
- [33] K. Momma and F. Izumi, VESTA 3 for three-dimensional visualization of crystal, volumetric and morphology data, *J. Appl. Crystallogr.* **44**, 1272 (2011).
- [34] Z. H. Li, S. Deng, M.-H. Whangbo, and H.-G. Luo, Orbital projection technique to explore the materials genomes of optical susceptibilities, *AIP Adv.* **12**, 055206 (2022).
- [35] Z. H. Li, A. Zhang, and H.-G. Luo, The microscopic origin of second harmonic generation response: The spatial structure of instantaneous dipole moments in electron excitation, *Angew. Chem. Int. Ed.* **61**, e202212125 (2022).
- [36] M. A. McGuire, H. Dixit, V. R. Cooper, and B. C. Sales, Coupling of crystal structure and magnetism in the layered, ferromagnetic insulator CrI<sub>3</sub>, *Chem. Mater.* **27**, 612 (2015).
- [37] H. Wang, V. Eyert, and U. Schwingenschlögl, Electronic structure and magnetic ordering of the semiconducting chromium trihalides CrCl<sub>3</sub>, CrBr<sub>3</sub>, and CrI<sub>3</sub>, *J. Phys.: Condens. Matter* **23**, 116003 (2011).
- [38] W. Song, G.-Y. Guo, S. Huang, L. Yang, and L. Yang, First-principles Studies of Second-Order Nonlinear Optical Properties of Organic-Inorganic Hybrid Halide Perovskites, *Phys. Rev. Appl.* **13**, 014052 (2020).
- [39] R. C. Miller, Optical second harmonic generation in piezoelectric crystals, *Appl. Phys. Lett.* **5**, 17 (1964).
- [40] S. Scandolo and F. Bassani, Miller's rule and the static limit for second-harmonic generation, *Phys. Rev. B* **51**, 6928 (1995).
- [41] M. Fiebig, V. V. Pavlov, and R. V. Pisarev, Second-harmonic generation as a tool for studying electronic and magnetic structures of crystals: Review, *J. Opt. Soc. Am. B* **22**, 96 (2005).
- [42] D. Sa, R. Valentí, and C. Gros, A generalized Ginzburg-Landau approach to second harmonic generation, *Eur. Phys. J. B* **14**, 301 (2000).
- [43] J. L. P. Hughes and J. E. Sipe, Calculation of second-order optical response in semiconductors, *Phys. Rev. B* **53**, 10751 (1996).
- [44] S. Sharma and C. Ambrosch-Draxl, Second-harmonic optical response from first principles, *Phys. Scr.* **2004**, 128 (2004).
- [45] R. W. Nunes and X. Gonze, Berry-phase treatment of the homogeneous electric field perturbation in insulators, *Phys. Rev. B* **63**, 155107 (2001).
- [46] M. Gajdoš, K. Hummer, G. Kresse, J. Furthmüller, and F. Bechstedt, Linear optical properties in the projector-augmented wave methodology, *Phys. Rev. B* **73**, 045112 (2006).
- [47] D. Xiao, G. B. Liu, W. Feng, X. Xu, and W. Yao, Coupled Spin and Valley Physics in Monolayers of MoS<sub>2</sub> and Other Group-VI Dichalcogenides, *Phys. Rev. Lett.* **108**, 196802 (2012).
- [48] H. B. Hu, K. Wang, H. Long, W. W. Liu, B. Wang, and P. X. Lu, Precise determination of the crystallographic orientations in single ZnS nanowires by second-harmonic generation microscopy, *Nano Lett.* **15**, 3351 (2015).
- [49] B. T. Fichera, A. Kogar, L. Ye, B. Gökce, A. Zong, J. G. Checkelsky, and N. Gedik, Second harmonic generation as a probe of broken mirror symmetry, *Phys. Rev. B* **101**, 241106(R) (2020).
- [50] M. Wu, Z. Li, and S. G. Louie, Optical and magneto-optical properties of ferromagnetic monolayer CrBr<sub>3</sub>: A first-principles GW and GW plus Bethe-Salpeter equation study, *Phys. Rev. Mater.* **6**, 014008 (2022).
- [51] M. Wu, Z. Li, T. Cao, and S. G. Louie, Physical origin of giant excitonic and magneto-optical responses in two dimensional ferromagnetic insulators, *Nat. Commun.* **10**, 2371 (2019).
- [52] S. Shree, D. Lagarde, L. Lombez, C. Robert, A. Balocchi, K. Watanabe, T. Taniguchi, X. Marie, I. C. Gerbe, M. M. Glazov, L. E. Golub, B. Urbaszek, and I. Paradisanos, Interlayer exciton mediated second harmonic generation in bilayer MoS<sub>2</sub>, *Nat. Commun.* **12**, 6894 (2021).
- [53] A. Strasser, H. Wang, and X. Qian, Nonlinear Optical and Photocurrent Responses in Janus MoSSe Monolayer and MoS<sub>2</sub>-MoSSe van der Waals Heterostructure, *Nano Lett.* **22**, 4145 (2022).